



Published in final edited form as:

Int J Mech Sci. 2020 April 15; 172: . doi:10.1016/j.ijmecsci.2019.105406.

Understanding of plasticity size-effect governed mechanical response and incomplete die filling in a microscale double-punch molding configuration

Bin Zhang[#], Mohammad S. Dodaran^{#1}, Shuai Shao¹, J. Choi, S. Park, W. J. Meng^{*}

Department of Mechanical & Industrial Engineering, Louisiana State University, Baton Rouge, LA 70803, U.S.A.

[#] These authors contributed equally to this work.

Abstract

Direct replication of microscale patterns onto metal surfaces by compression molding with patterned dies is used to fabricate metal-based structures for microsystem applications. Micron scale plasticity governs both the mechanical molding response and the geometric fidelity of replicated patterns. Microscale molding replication offers a technologically relevant example in which various plasticity size effects manifest themselves and control the effectiveness of the fabrication process.

Microscale compression molding of a single-crystal Al specimen was studied by combining experimentation with conventional and strain gradient plasticity finite element simulations. In the single-punch molding configuration, single rectangular punches with different widths and lengths were used. In the double-punch configuration, two identically-dimensioned rectangular punches with a spacing in between were used. Under single-punch molding at the micron scale, both the absolute punch width as well as the length-to-width ratio affected the characteristic molding pressure. Under double-punch molding, both the measured characteristic molding pressure and the material flow to fill the gap between the two rectangular punches exhibited a significant dependence on the spacing to punch-width ratio and—when this ratio was fixed—on the absolute spacing between punches. The present study elucidates the impact of plasticity size effects on the efficacy of pattern replication by molding at the micron scale.

^{*} Author to whom all correspondences should be addressed (wmeng1@lsu.edu).

¹Current affiliation: Department of Mechanical Engineering, Auburn University, Auburn, AL, 36849, U.S.A. and National Center for Additive Manufacturing Excellence (NCAME), Auburn University, Auburn, AL 36849, U.S.A.

6. Disclaimer

This report, in part, was prepared as an account of work sponsored by an agency of the United States Government. Neither the United States Government nor any agency thereof, nor any of their employees, makes any warranty, express or implied, or assumes any legal liability or responsibility for the accuracy, completeness, or usefulness of any information, apparatus, product, or process disclosed, or represents that its use would not infringe privately owned rights. Reference herein to any specific commercial product, process, or service by trade name, trademark, manufacturer, or otherwise does not necessarily constitute or imply its endorsement, recommendation, or favoring by the United States Government or any agency thereof. The views and opinions of authors expressed herein do not necessarily state or reflect those of the United States Government or any agency FA R&D Special TC NOVEMBER 2017- FF Page 4 of 12 thereof.

Keywords

mechanical size effects; pattern replication; micro molding; incomplete die filling; strain gradient plasticity

1. Introduction

Fabricating surface patterns at nano/micro dimensions offers a means for achieving structures with potential usage in wide ranging technological applications, including photonic devices [1], electronic devices [2], micro chemical reactors [3], and micro heat exchangers [4]. This paper deals with the understanding of how plasticity size effects influence the fabrication of microscale patterns on metal surfaces.

From the early 1980s to the present time, two different techniques for replicating micro/nano scale patterns onto solid surfaces from pre-fabricated dies have been devised and studied. In LiGA microfabrication (**L**ithographie, **G**alvanoformung, **A**bformung) [5], microscale imprinting with electrodeposited Ni dies is used to impart intermediate surface patterns onto a thick polymeric resist supported on a backing plate, followed by metal electrodeposition into patterned recesses on the resist. In nanoimprinting lithography (NIL) [6], a nanostructured hard die is pressed into a thin layer of polymeric resist on a substrate to impart intermediate nanoscale surface patterns on the resist, followed by reactive ion etching into the substrate. Common to both LiGA and NIL, creation of the intermediate surface pattern proceeds by pressing a patterned hard die into polymeric materials above their glass transition temperatures, causing viscous flow into die recesses. Formation of nano-/micro-scale patterns occurs after cooling to below the polymer glass transition temperature followed by demolding.

In contrast to LiGA and NIL, a final microscale pattern can be transferred directly onto metal surfaces by compression molding with structured hard dies. Such direct microscale pattern replication by molding have been demonstrated in Al [7], Cu [8], and Ni [9]. Direct molding replication creates patterns on metal surfaces in high throughput and forms the basis for fabricating metal-based microscale structures usable in various micro devices, e.g., microchannel heat exchangers with significant cooling powers [10] and complex geometries [11]. In direct molding replication, formation of the desired final microscale surface pattern involves plastic flow of metals into die recesses under compression, without the need for an additional processing step. The mechanical response of the molded material and the geometrical fidelity of the replicated pattern are both controlled by micron scale plasticity.

Plastic deformation at small length scales, from $\sim 1000\ \mu\text{m}$ to sub- μm , has been intensely researched in the past two decades, revealing both strain-gradient and non-strain-gradient related size effects. Significant and non-monotonic dependence of flow stress on size has been observed on metallic specimens with external sizes ranging from $\sim 1000\ \mu\text{m}$ and above to $\sim 1\ \mu\text{m}$ and below [12]. With strain gradients, significant strengthening has been observed when strain gradients are imposed by the deformation geometry, such as in torsion of thin wires [13] and bending of thin foils [14]. Without strain gradients, significant strengthening has also been observed in axial compression of pillars when their diameters decrease from

~40 μm down to ~0.2 μm [15]. In contrast, softening was observed in uniaxial compression tests on specimens with characteristic dimensions ranging from ~3000 μm down to ~200 μm [12,16,17]. Distinct from the simple deformation geometries such as wire torsion, foil bending, and pillar compression, microscale molding replication in metals offers a technologically relevant example involving complex plastic flow, where micron scale plasticity of metals assumes a controlling role in determining the effectiveness of the fabrication technique. Formation of nano/micro scale surface patterns through compression of hard dies into metal surfaces can also be a part of other small scale metal forming operations, such as progressive microforming [18].

Mechanical response and geometrical fidelity of the replicated pattern to the original die are of central importance in microscale pattern replication by molding. One particular concern in molding replication is whether the material being molded is able to completely fill the die recesses during the molding process, especially when multiple recesses are of different dimensions. One case in point is shown in Fig. 1(a), which displays a typical result of elemental Al after being molded with a micron scale patterned Si die, containing a one-dimensional periodic array of long rectangular punches. As shown in Fig. 1(a), the height of Al flow into the recesses between individual Si punches is far less than the total punch displacement into the molded Al piece. To exaggerate, the entire Si die appeared to have sunk into the molded Al as if a solid piece, with little material flowing up to fill the gaps among individual Si punches. Such a result of compression molding is evidently not satisfactory when the goal is to imprint in parallel multiple geometrical features onto the surface of the molded piece. To our knowledge, this phenomenon, although clearly relevant to fabrication of surface patterns by molding replication, has not been properly understood, especially when the characteristic dimension goes to the micron scale.

In this paper, we provide new data and a better understanding of material's response to microscale compression molding by a hard die containing protrusions/recesses of different dimensions. To study the degree of die filling achieved, a simplified deformation geometry was chosen: a single-crystal Al specimen was compression molded by tool steel dies in the form of two parallel rectangular punches of nominally the same dimensions separated by a spacing between them (see Fig. 1(b)). In this geometry, dubbed "double-punches", we have systematically varied the punch width, w , and spacing, s . Detailed experimentation is accompanied by conventional and strain-gradient plasticity finite element (FE) simulations. In what follows, Section 2 describes the procedures for experimentation and simulation. Section 3 presents the major results and a discussion, and Section 4 gives a summary.

2. Procedures for experimentation and simulation

An FEI Quanta3D FEG Dual-Beam scanning electron microscope/focused ion beam (SEM/FIB) instrument was used to fabricate two series of rectangular strip punches in a tool steel, with a bulk hardness of ~HRC60. Commercially available 1 mm diameter tool steel rods were mechanically polished at one end to reduce its diameter to 50–100 μm . The final cutting step was accomplished on the FIB instrument, using a Ga^+ ion beam current of 1 nA to polish the top and sidewall surfaces of each punch. A series of single, rectangular, strip punches were first cut, with values of their widths, w , of ~13 μm , ~8 μm , ~4 μm , ~2 μm , and

$\sim 1 \mu\text{m}$. The length of each punch, L , was at least $3w$, such that compression molding with these punches can be considered to occur under approximately plane-strain conditions. The morphology of FIB-cut single rectangular punches is illustrated in Section S1 of Supplemental Materials.

A number of double-punches were then cut. The dimensions of several different series of double-punches are summarized in Table 1, where s represents the spacing between two rectangular punches of the same nominal dimensions, w represents the width of each rectangular punch, and L represents the length of each rectangular punch. We define a parameter λ as the ratio s/w and another parameter α as the ratio L/w . Table 1(a) shows the dimensions of five double-punches. Each double-punch has the same s of $\sim 2 \mu\text{m}$, with w decreasing from $\sim 17.0 \mu\text{m}$ to $\sim 4.2 \mu\text{m}$, such that λ varies from 0.12 to 0.48. Table 1(b) shows the dimensions of another four double-punches, keeping λ fixed at ~ 0.20 , while varying the absolute dimensions of s and w proportionally. As s increases from $\sim 1.0 \mu\text{m}$ to $\sim 4.5 \mu\text{m}$, w increases correspondingly from $\sim 5.0 \mu\text{m}$ to $\sim 22.5 \mu\text{m}$. Table 1(c) shows the dimensions of six double-punches, keeping w fixed at $\sim 5 \mu\text{m}$ and varying s from $\sim 1.0 \mu\text{m}$ to $\sim 7.5 \mu\text{m}$, with λ increasing correspondingly from 0.20 to 1.5. Table 1(d) shows the dimensions of another three double-punches, with varying w and s values and corresponding λ values increasing from 1.0 to 2.2. Figure 1(b) shows an SEM image of one typical double-punch, with $L \sim 67 \mu\text{m}$, $w \sim 22.5 \mu\text{m}$ and $s \sim 4.5 \mu\text{m}$. Through images shown in Supplemental Materials Section S1 and Fig. 1(b), together with similar ones not shown, FIB-cut tool steel single and double punches are seen to possess straight edges, sharp corners, and relatively smooth sidewalls.

The so-fabricated single-punches and double-punches were then used to conduct instrumented compression molding on one $\langle 110 \rangle$ oriented, single-crystal Al specimen (MTS Systems Corp., Knoxville, TN), polished to a mirror finish. All compression molding experiments were carried out on a Nanointenter XP system (MTS Systems Corp., Knoxville, TN), in a displacement-controlled mode. In all molding runs, the displacement rate was set to 10 nm/sec. Each molding experiment was repeated at least 4 times at room temperature. Raw molding response data consisted of the total compression force, P , vs. the total punch displacement, δ_{total} . Because δ_{total} includes a load frame stiffness contribution, separate calibration runs were made to determine the actual punch penetration into the Al specimen, δ , following previously published procedures [19]. Further details on the conversion of raw P - δ_{total} curves to P - δ curves are shown in Section S1 of Supplemental Materials.

Repeat P - δ curves obtained at each punch width were averaged together. The nominal contact pressure, p , was obtained by normalizing the total force P by the nominal contact area. The indentation depth, δ , was normalized by the punch width. For single- and double-punch molding, nominal contact areas were taken as $L \times w$ and $2 \times L \times w$, respectively. Similarly, punch widths were taken as w and $2w$ for single- and double-punch molding, respectively. For single-punch molding, the conversion from P - δ curves to p - δ/w curves, with $p = P/(L \times w)$, enables quantitative comparison of molding response data obtained from punches of different dimensions [19, 20, 21]. For double-punch molding, the conversion P - δ curves to p - $\delta/2w$ curves, with $p = P/(2 \times L \times w)$, achieves a similar normalization. All the

molding response curves obtained from single- and double- punch compression were processed following the same procedure outlined above.

The present molding experiments measure the total molding force P , and do not generate any direct information on the friction between the punch and the molded material. Presently prevailing methods for assessing friction in macroscale metal forming, such as the ring compression test (RCT) [22] and the double cup extrusion test (DCET) [23], are indirect and becomes increasingly difficult to execute as the characteristic dimension of forming operations decreases to the sub-mm and micron scales. In this work, the influence of friction on the material's response to single- and double- punch molding was not evaluated, although we note that all molding experiments were conducted under dry contact conditions and the friction between the punch and the molded Al is not expected to vary.

Because of the single crystal nature of the Al specimen, it is of interest to inquire whether the measured molding response using the long rectangular strip punch depends on the in-plane orientation of the punch long axis. Multiple sets of molding runs were performed using one single rectangular strip punch, rotating the in-plane orientation of the punch long axis. As detailed in Section S1 of Supplemental Materials, the in-plane orientation of the punch long axis had a minimal effect on the molding response of the single-crystal Al specimen. Further experimentation showed that the in-plane orientation of the punch long axis also had a minimal effect on the molding response and morphology of molded features in the double-punch case. This apparent in-plane isotropic molding response, together with the fact that all single- and double- punch molding experiments were conducted on the same $\{110\}$ face of the Al crystal, suggests that crystal anisotropy is not the dominant factor controlling the observed material response in the present microscale single- and double-punch molding experiments. Consequently, in the associated modeling work, isotropic conventional and strain-gradient plasticity FE simulations were conducted and an explicit consideration of crystal anisotropy was not taken.

Morphological examinations of molded features were carried out using the same FEI Quanta3D FEG SEM/FIB instrument. Atomic force microscopy (AFM) was also used for quantitative measurements on molded features. An Agilent Technologies 5500 Scanning Probe Microscope was operated in an intermittent contact mode, typically referred to as an AC mode, with a scan range of $15\ \mu\text{m} \times 15\ \mu\text{m}$ at 512×512 pixels and a scan rate of 0.5 Hz. Specimens were imaged in air at room temperature and humidity. Tapping-mode silicon cantilever probes (NanoSensors type PPP-RT-NCHR) were used, with a nominal resonance frequency of 330 kHz, a nominal constant force of 42 N/m, and a curvature radius of less than 10 nm. Image processing and analysis were carried out using Gwyddion 2.53 and consisted of a background correction. Additional optical profilometry (OP) measurements were carried out on a Bruker GTK series optical profilometer. Raw OP data were processed by the Vision64 map software.

FE simulations of both single- and double- punch molding, including both 3D and 2D (plane-strain) cases, were performed with conventional plasticity (CP) and strain-gradient plasticity (SGP) models. For clarity, the FE simulations performed are summarized in Table 2. The model setup and mesh geometries are shown in Fig. 2. For 2D (plane-strain) double-

punch simulations, a mesh shown in Fig. 2(a) was used with symmetric boundary conditions applied in the x-direction to reduce the computational cost. Symmetric boundary conditions were also applied to the bottom surface. In these simulations, the punch width was kept constant at $w = 46.75 \mu\text{m}$, while the other parameters such as λ and the intrinsic material length scale parameter (l) were varied (see Table 2(a)). The corners of the punch have a fillet size of $r = 2.0 \mu\text{m}$ to help the implicit simulations converge. Coarse mesh with element size of $\sim 200 \mu\text{m}$ was created away from the punch, while fine mesh was created near the punch. The size of the simulation cell is $1400 \mu\text{m}$ on all sides. A convergence study has been performed using a 2D plane-strain double punch case with $\lambda = 2.2$ to determine the appropriate size of the fine elements. As shown in Section S2 of Supplemental Materials, starting with a mesh size of $A_1 = 6.4 \mu\text{m}$ near the punch, the element size has been incrementally halved ($A_K = A_1/2^n$, where $K = 2^n$ and n is a non-negative integer) to investigate the error convergence behavior of the simulations. The error is quantified by the terminal load experienced by the punch at a penetration depth of $d = 8.6 \mu\text{m}$, using the terminal load for $K = 64$ as a reference. The error convergence is achieved when $K = 8$, to a value of $< 0.03\%$. The corresponding element size, $A_8 = 0.8 \mu\text{m}$ was used for all 2D plane-strain simulations. For 3D simulations, an even smaller mesh size of $A = 0.5 \mu\text{m}$ was used. An additional convergence study on the uniform implicit “timestep” has also been performed for 2D simulations with the strain gradient plasticity model, with further details given in Section S2 of Supplemental Materials. As listed in Table 2(b), for the 3D single-punch simulations, three single-punches with different aspect ratios were modeled, maintaining $w/2 = 5.5 \mu\text{m}$. In 3D double-punch simulations, another three aspect ratios were considered, maintaining $w = 5.5 \mu\text{m}$. There was a fillet of $r = 2 \mu\text{m}$ on all edges of the punch in contact with the specimen. In these 3D simulations (see Figs. 2(b) and 2(c)), to conserve computational resources, only a quarter of the actual loading geometry was modeled. In x and z directions, symmetric boundary condition was applied to all lateral surfaces, while in y direction, symmetric boundary condition was applied only to the bottom surface. The top loading surface in y was left free. The size of the 3D simulation cell was $1500 \mu\text{m}$ on all sides. For 2D simulations, the element type used was 8-node biquadratic plane strain quadrilateral with reduced integration (ABAQUS designation CPE8R). For 3D simulations, the element type used was 10-node quadratic tetrahedral (ABAQUS designation C3D10).

The simulations were performed using ABAQUS[®]. In addition to CP simulations, an SGP model [24] was applied to 2D plane-strain simulations via the UMAT developed by Martínez-Pañeda et al. [25]. According to the adopted SGP model, the flow stress at a given plastic strain (ϵ^p) and effective plastic strain gradient (η^p) is given as,

$$\sigma_{flow} = \sigma_{ref} \sqrt{f^2(\epsilon^p) + l\eta^p}, \quad (1)$$

where $\eta^p = 0.5 \sqrt{\eta_{ijk}^p \eta_{ijk}^p}$ with the plastic strain gradient tensor defined as

$$\eta_{ijk}^p = \epsilon_{ik,j}^p + \epsilon_{jk,i}^p - \epsilon_{ij,k}^p, \text{ and } l \text{ is the intrinsic material length scale. In Eq. (1),}$$

$\sigma_{ref} = \sigma_Y (E/\sigma_Y)^N$ and $f(\epsilon^p) = (\epsilon^p + \sigma_Y/E)^N$ such that the conventional power hardening law

$$\sigma = \sigma_Y \left(1 + \frac{E\epsilon^p}{\sigma_Y}\right)^N \text{ is recovered when } l = 0. \text{ The } l \text{ parameter is also a measure of the}$$

material's sensitivity to the existence of strain gradients. Here, σ_Y is the yield stress, N is the strain hardening exponent, and E is the Young's modulus. Setting $l = 0$, the choice in the values of material parameters given in Table 3 results in the flow stress – plastic strain relation shown in Fig. 2(d) under a gradient-free condition.

According to Huang et al. [24], the l parameter for FCC metals is given as

$$l = 18\beta^2 \left(\frac{\mu}{\sigma_{ref}} \right)^2 b, \quad (2)$$

where β is an empirical coefficient with a value between 0.3 to 0.5, μ is the shear modulus, b is the magnitude of the Burgers vector ($b = 2.86 \text{ \AA}$ for Al). According to the parameters given in Table 3, $l = 12 \text{ \mu m}$ for Al with β taken as 0.5. In SGP FE simulations, a parametric study on l was performed, with varying l values of 0, 0.25, 1, 3, 5.9, 11.8, and 17.7 μm . For CP FE simulations, the flow stress – plastic strain relation shown in Fig. 2(d), with material's parameters given in Table 3 and l taken as 0, was used as the input for simulating the material's plastic response.

3. Results and discussion

3.1 Mechanical size effect in molding with single long rectangular strip punches

Figure 3(a) summarizes the averaged compression molding response curves, p - L/w , obtained from the single-crystal Al specimen with single long rectangular punches with widths w decreasing from $\sim 13 \text{ \mu m}$ to $\sim 1 \text{ \mu m}$. All measured p - L/w curves are qualitatively similar, with an initial section in which p increases sharply with increasing L/w , followed by a “knee” after which p increases more slowly in an approximately linear fashion as L/w increases further. The molding response curves at w values of 13 μm , 8 μm , and 4 μm are almost on top of each other. As w decreases further from 4 μm to 1 μm , the p - L/w curves become stiffer, indicating that p has an explicit and significant dependence on w , contrary to conventional continuum mechanics expectations and indicative of the presence of a significant mechanical size effect. To better quantify the mechanical size effect as the width of the single punch decreases, the p value at $L/w = 0.25$ was taken as the characteristic molding pressure, p_c , and plotted as a function of w in Fig. 3(b). The so-obtained characteristic molding pressure remains relatively flat at $w > 4 \text{ \mu m}$, and increases significantly as w decreases from 4 μm to 1 μm . The findings summarized in Fig. 3 is consistent with previous experimental observations [19]. To eliminate possible complications associated with this mechanical size effect in single punch molding, in subsequent double-punch molding runs, individual punches were fabricated with w close to or above 4 μm .

As expected, FE simulations with conventional plasticity model could not capture the effects of varying the absolute punch width, w . Instead, a dependence of the mechanical response on the punch aspect ratio was captured. Figure 4(a) shows the results of CP FE simulations, which show that p depends on the punch aspect ratio, $\alpha = L/w$. Figure 4(a) shows that p decreases as α increases and that, when α is greater than ~ 2 , the effects of α diminish. Since $\alpha > 3$ was maintained in all experiments, this precludes the possibility that the dependence

of p_c on w , shown in Fig. 3(b), arises from variations in α . It is noted that the effect of α on the contact pressure, shown in Fig. 4(a), is a manifestation of the corresponding variation in the stress tri-axiality underneath the punch. As a measure of the stress tri-axiality, Fig. 4(b) shows the distribution of pressure ($p = -1/3 \sigma_{ii}$) on the x - y plane as well as along the y -axis. A lower α value corresponds to a significantly higher pressure immediately below the punch. This higher pressure translates to the stiffer p - $/2w$ curve observed when $\alpha = 1$.

3.2 Double-punch molding: mechanical response and incomplete die filling

Figure 5 summarizes experimental double-punch molding response curves, p - $/2w$, measured using double-punches described in Table 1. All the molding response curves are qualitatively similar to those obtained from single-punch molding, i.e., each curve includes an initial section where p increases rapidly with increasing $/2w$, followed by an abrupt turn-over after which p increases more slowly with further increases in $/2w$. Specifically, Fig. 5(a) summarizes the molding response curves obtained using the series of double-punches described in Table 1(a), with a constant spacing s of $\sim 2 \mu\text{m}$, while the width of the individual rectangular punch w varied from $17 \mu\text{m}$ to $4.2 \mu\text{m}$. The value of $\lambda = s/w$ varied correspondingly from 0.12 to 0.48. Figure 5(a) shows nearly identical molding response curves at λ of 0.12 and 0.15. As λ increases further, the molding response curves become stiffer, i.e., a clear increase in p is observed. Figure 5(b) shows the p - $/2w$ curves obtained using the series of four double-punches described in Table 1(b), with a constant λ of 0.2, while s changed from $1.0 \mu\text{m}$ to $2.0 \mu\text{m}$, $3.2 \mu\text{m}$, and $4.5 \mu\text{m}$. The molding response curves is seen to depend on the absolute value of s : p increases as s decreases from $\sim 4.5 \mu\text{m}$ to $\sim 2 \mu\text{m}$. The p - $/2w$ curves for s equals $1.0 \mu\text{m}$ and $2.0 \mu\text{m}$ are nearly identical, and significantly exceed those for s of $3.2 \mu\text{m}$ and $4.5 \mu\text{m}$. Figure 5(c) shows the molding response curves obtained from the three double-punches described in Table 1(c), with a constant w of $\sim 5 \mu\text{m}$ and changing s values of $1.0 \mu\text{m}$, $1.5 \mu\text{m}$, and $2.4 \mu\text{m}$, and corresponding λ values of 0.20, 0.29 and 0.48. It is evident that the response curves exhibit a similar trend as shown in Fig. 5(a), namely, p increases with increasing λ . Figure 5(d) shows the molding response curves using the other three double-punches described in Table 1(c), with a constant w of $\sim 5 \mu\text{m}$ and changing s values of $3.50 \mu\text{m}$, $5.2 \mu\text{m}$, and $7.5 \mu\text{m}$, and corresponding λ values of 0.67, 1.0, and 1.50. Now a clear and opposite trend can be observed, that p begins to decrease as λ increases further. Figure 5(e) summarizes the molding response curves obtained from another three double-punches described in Table 1(d), with λ varying from 1.0 to 2.2. A similar trend as shown in Fig. 5(d) was observed, in that p decreases as λ increases, and the molding response curves corresponding to λ of 1.8 and 2.2 are almost on top of each other.

The characteristic molding pressure for double-punch molding is again defined by taking (or extrapolating) the measured p value at (to) $/2w = 0.25$. It should be noted from Table 1 that the double-punches have different length-to-width ratios, $\alpha = L/w$, with α values ranging from ~ 3.0 to ~ 6.5 . To better understand the effect of α on the molding response, three additional double-punches, with the same $w \sim 7.2 \mu\text{m}$, $s \sim 3.6 \mu\text{m}$, and $\lambda = 0.5$ but varying α values of ~ 5.6 , ~ 4.4 , and ~ 3.3 , were fabricated and then used to conduct molding experiments. Table 4 lists the specific punch dimensions, and their corresponding SEM images are shown in Section S3 of Supplemental Materials. Figure 6(a) shows the molding response curves obtained using the three double-punches described in Table 4, with four

repeat molding runs conducted with each punch. The molding response curves at $\alpha \sim 3.3$ are stiffer as compared to those at $\alpha \sim 4.4$ and ~ 5.6 . Figure 6(b) plots as a function of α the corresponding characteristic molding pressure, p_c , again by taking measured p values at $z/2w = 0.25$. The error bars stem from averaging p_c values obtained from repeat molding runs. Figure 6(b) shows that p_c values approach a constant at α values of ~ 4.4 and ~ 5.6 , ~ 407 MPa, whereas at $\alpha \sim 3.3$, the p_c value is ~ 430 MPa, $\sim 5\%$ higher than those corresponding to $\alpha > 4$. Corresponding FE simulations (described in Table 2(b)) using CP confirm the trend observed in the experiments, as shown in Fig. 6(c). A significant reduction in the pressure-depth response is witnessed when α increases from 2 to 4.36 (α of 2.36). From $\alpha = 4.36$ to $\alpha = 7.33$ (α of nearly 3), the resulting variation in the pressure-depth response is substantially less. The softened responses associated with the larger α values are, at least in part, also due to the change of stress tri-axiality beneath the punches.

Figure 7(a) plots all measured double-punch characteristic molding pressure values, p_c , as a function of $\lambda = s/w$. To eliminate the influence of the punch aspect ratio on p_c values, p_c obtained from double punches with $\alpha > 4$ were multiplied by a factor of 1.05, assuming that the same punch aspect ratio effect on p_c , described in Fig. 6(b), applies to other double-punch molding results with different w and s values. Error bars on p_c again stem from averaging results from repeat molding runs. The four black data points in the “ $s=2\mu\text{m}$ ” data group are obtained from the molding response curves shown in Fig. 5(a). The p_c value at $\lambda \sim 0.12$ is ~ 370 MPa and changes little as λ increases from 0.12 to 0.15. It then jumps to ~ 395 MPa at $\lambda \sim 0.20$, and continues to increase to ~ 423 MPa at $\lambda \sim 0.31$ and ~ 442 MPa at $\lambda \sim 0.48$. The five red data points in the “ $w=5\mu\text{m}$ ” data group correspond to the molding response curves shown in Figs. 5(c) and 5(d). The measured characteristic pressure increases from ~ 395 MPa to ~ 450 MPa as λ increases from 0.20 to 0.48. Moreover, at each λ value, this characteristic pressure is close to the corresponding data points in the “ $s=2\mu\text{m}$ ” data group. The p_c value decreases, after reaching a maximum value of ~ 450 MPa, to ~ 425 MPa at $\lambda = 1.5$. The three dark green data points in Fig. 7(a) in the “ $\lambda > 1.0$ ” data group come from molding response curves shown in Fig. 5(e). The p_c value reduces gradually as λ increases from 1.0 to 2.2. One magenta data point at $\lambda = 0.5$ is obtained from the aforementioned additional double-punch with $w \sim 7.2 \mu\text{m}$, $s \sim 3.6 \mu\text{m}$, and $\alpha \sim 3.3$.

Focusing on the four blue data points in the “ $\lambda = 0.20$ ” data group in Fig. 7(a), obtained from the molding response curves shown in Fig. 5(b), the two points with $p_c \sim 395$ MPa largely overlap the black and red data points in the “ $s=2\mu\text{m}$ ” and “ $w=5\mu\text{m}$ ” data group, while the other two blue data points lie below with lower characteristic pressures. Because w values in these double-punch sets were deliberately chosen to eliminate possible mechanical size effects due to single punch molding, as exhibited in Fig. 3(b), the measured p_c variation at a constant λ of 0.2 from ~ 350 MPa to ~ 395 MPa, a change of $\sim 13\%$, can only be attributed to variation in the absolute spacing between two punches, s . In other words, the measured characteristic pressure for double-punch molding is not only λ dependent, but also s dependent at a constant λ when s becomes sufficiently small. According to conventional continuum mechanics, mechanical response to molding by a long double-punch set should depend only on the relative size of s and w , i.e., λ , but not on the absolute value of s . This presently observed dependence of p_c on s at a constant λ thus signifies a different manifestation of mechanical size effect as the characteristic molding dimension approaches

the micron scale: in this instance, the controlling size is the gap between two punches, even when the width of the individual punch is sufficiently large so a mechanical size effect is not evident in single-punch molding.

Corresponding to the experimental results shown in Fig. 7(a), 2D plane-strain FE simulations of double-punch molding with both CP and SGP (described in Table 2(a)) were performed, with results shown in Fig. 7(b). Both 2D CP and SGP simulations used an identical punch width of $w = 46.75 \mu\text{m}$ and, when λ varies from 0.12 to 2.2, correspond to s values of $5.61 \mu\text{m}$ to $102.85 \mu\text{m}$. As a confirmation of the correctness of the FE simulations, the characteristic molding pressure predicted by SGP FE at $l = 0 \mu\text{m}$ reproduces the predictions made by CP FE. It is apparent that the p_c value from both CP and SGP FE simulations exhibits a monotonically increasing trend with increasing λ . The p_c value increases faster with increasing λ as the intrinsic material length scale parameter l is increased. The saturation of p_c at higher λ values is also delayed with increasing l . In all FE simulations, the experimentally observed peak in p_c at λ of ~ 0.5 , shown in Fig. 7(a), was not present, suggesting an origin for this peak other than SGP. Exact mechanism responsible for this observed peak in p_c is not understood at this moment.

Besides the measured mechanical response in double-punch molding, as summarized in Figs. 5 and 7 including a mechanical size effect manifestation, the phenomenon of incomplete die filling is also evident in the micron scale double-punch molding experiments. Figures 8(a), 8(b), and 8(c) show SEM images of three imprints made on the single-crystal Al specimen, arising from molding using the double-punch shown in Fig. 1(b), with $w = 22.5 \mu\text{m}$ and $s = 4.5 \mu\text{m}$. The three imprints were made at indentation depths of $\sim 3.5 \mu\text{m}$, $\sim 8.8 \mu\text{m}$, and $\sim 11.8 \mu\text{m}$, respectively, as measured from the edge heights of the three imprints. All three imprints have flat bottoms, sharp corners, and clean sidewalls. Fine features present on the bottoms of the imprints mimic the features on the punch top surfaces generated during the FIB cutting process, shown in Fig. 1(b). From Fig. 8(a), it is evident that the height of Al flow into the gap between the two punches fell far short of the entire indentation depth, and only a long shallow bump was formed along the gap location. This incomplete gap filling persisted as s increased, as evident in Figs. 8(b) and 8(c). End effects are present, most evident in Fig. 8(c), which shows that the height of the long bump, h , is the largest at the two ends of the double-punch, and approaches a constant near the center portion where the condition of plane-strain is best satisfied.

To better quantify these observations, AFM measurements were conducted over $15 \mu\text{m} \times 15 \mu\text{m}$ scan areas. The AFM scan areas were placed respectively in the centers of the imprints shown in Figs. 8(a)–8(c), as indicated schematically by the red square shown in Fig. 8(a). Corresponding topographic AFM images are shown in Figs. 8(d), 8(e), and 8(f), presented in 2D top views. The corresponding height profiles, taken along line scans perpendicular to the long bumps, are shown respectively in Figs. 8(g), 8(h), 8(i) and yield a value of the bump height h for each indentation depth s . Table 5 summarizes these results, and shows that even with a more than three-fold increase in s , the ratio of bump height at the center of the imprint to the indentation depth or the gap filling ratio, h/s , remains at 10% or below. Phenomena similar to what is shown in Fig. 8 were observed with other microscale double-punches with $\lambda < 0.20$, indicating that the Al specimen molded by two long rectangular

punches separated by a gap behaves—in effect—as if it were compressed by a single punch with a width of $2w+s$. As indicated in the introduction, such incomplete die filling is detrimental to the technical goal of simultaneously replicating multiple patterns by molding.

To quantify the degree of gap filling in double-punch molding when the gap dimension s increases from the micron scale to the mm scale, a much larger tool steel double-punch was fabricated by wire electrical discharge machining (EDM), with $w \sim 2$ mm, $s \sim 0.4$ mm, and $l \sim 8$ mm. Figure 8(j) shows an SEM image of one imprint made in a large grain polycrystalline Al specimen, as the single-crystal Al specimen was too small for this particular double-punch. An incomplete gap filling was also observed in this case, qualitatively similar to the microscale case shown in Figs. 8(a)–8(i). Figures 8(k) and 8(l) show results of optical profilometry (OP) measurements in areas schematically designated as 1 and 2 in Fig. 8(j). Figure 8(k) shows the height of the bump along the gap location is $h = 145$ μm . The indentation depth was obtained from the OP measurements shown in Fig. 8(l) to be 230 μm . Additional molding runs using this double-punch were performed, with results summarized in Table 5. Examination of entries in Table 5 reveals that the degree of gap filling, h/d , is significantly higher at the mm scale as compared to that at the micron scale, with the average value of all h/d entries for the macroscale case, ~ 0.50 , higher than the average for the microscale case, ~ 0.09 , by ~ 5.5 . Noting that $\lambda = 0.2$ for both the micron and mm scale double-punches, the present results on gap filling, summarized in Fig. 8 and Table 5, offer another manifestation of the mechanical size effect: a substantially less degree of material flow occurs to fill the gap between two punches at the micron scale as compared to the mm scale, at identical relative dimensions, i.e., identical λ .

The SEM images of three double-punches described in Table 1(c), with w of ~ 5 μm and varying s of 1.0 μm , 3.5 μm , and 5.2 μm , are given in Section S3 of Supplemental Materials. Double-punch molding runs performed with these three double-punches illustrate the influence of s and λ on the degree of gap filling during double-punch molding. SEM images of imprints created on the single-crystal Al specimen are shown respectively in Figs. 9(a), 9(b), 9(c). As shown in Fig. 9(a), at $s \sim 1.0$ μm and $\lambda = 0.2$, the molded Al did not fill the gap between the two punches, forming only a long bump at the gap location with the bump height $< 10\%$ of the punch indentation depth, consistent with the results shown in Fig. 8. As s increases to 3.5 μm and λ to 0.67, Fig. 9(b) shows that the bump height increased to $\sim 60\%$ of d , more substantially but still not completely filling the gap. As s increases further to 5.2 μm and λ to 1.0, the Al flow into the gap between two punches reaches almost 100% of d , as shown in Fig. 9(c). Contrasting results shown in Fig. 9(c) with the micron scale double-punch case shown in Fig. 8, the degree of gap filling during double-punch molding is seen to depend not only on the absolute dimension of s , but also on the value of λ .

The incomplete filling of the gap between the two punches at small λ is not unique to small s cases. Indeed, 2D simulations with CP and SGP at $l = 0$ μm (described in Table 2(a)) also reveal incomplete filling at small λ , as evidenced by the magenta curves shown in Figs. 9(d)–9(f). Without a strain gradient contribution, the incomplete filling originates in part from the interaction between the stress fields generated by the two neighboring punches. To illustrate, Fig. 10 plots the stress distribution below double-punches with different $\lambda = s/w$,

according to the plane-strain isotropic elastic solution for a single rectangular long punch of width $2a$ as given by Ref. [26] (as shown in Fig. 10(a)):

$$\begin{aligned}\sigma_x &= -\frac{2Py}{\pi^2} \int_{-a}^a \frac{(x-t)^2}{\sqrt{a^2-t^2}[(x-t)^2+y^2]^2} dt, \\ \sigma_y &= -\frac{2Py^3}{\pi^2} \int_{-a}^a \frac{1}{\sqrt{a^2-t^2}[(x-t)^2+y^2]^2} dt, \\ \sigma_z &= \nu(\sigma_x + \sigma_y), \\ \tau_{xy} &= -\frac{2Py^2}{\pi^2} \int_{-a}^a \frac{(x-t)}{\sqrt{a^2-t^2}[(x-t)^2+y^2]^2} dt,\end{aligned}\quad (3)$$

where P is the load per unit length in the direction perpendicular to x - and y - axis, x and y are the coordinate of a material point beneath the punch, t is the integration variable over the punch width (from $-a$ to a), and ν is the Poisson's ratio (assumed to be 0.3 in this work). The units for length, load, and pressure are $10 \mu\text{m}$, 0.1 N , and 1 GPa , respectively. The solution for the elastic stress distribution below a double-punch was obtained by superimposing two single-punch solutions.

As shown by Figs. 10(b)–10(e), the shear stresses τ_{xy} generated by the two adjacent corners of the two punches are opposite in sign. As the stress fields of the two punches couple, the resultant shear stresses cancel to some extent. As a result, the resultant von Mises stress in the region between two closely-spaced punches is substantially lower than that in the regions near the external punch corners, as shown in Figs. 10(f)–10(i). This reduced von Mises stress in the gap region therefore reduces the driving force for plastic deformation of the material between the two punches, contributing to incomplete gap filling.

The strain gradient plastic response of materials does, however, substantially add to the incomplete gap filling at the micron scale. According to SGP, materials harden in the presence of strain gradients. As shown in Figs. 9(d)–9(f), the increase in the intrinsic material length scale parameter l significantly exacerbates the incomplete gap filling. A complete simulation data set on the fill ratio (h') vs. λ at $w = 8.6 \mu\text{m}$ and $w = 46.75 \mu\text{m}$ has been provided in Fig. 11(a). It appears that the degree of gap filling starts to deteriorate as the l parameter approaches the absolute gap spacing s . For instance, at $s = 5.61 \mu\text{m}$ ($\lambda = 0.12$, Fig. 9(d)), a reduction in the fill ratio by $\sim 50\%$ (h' from 0.138 to 0.064) is achieved at $l = 5.9 \mu\text{m}$; at $s = 54.23 \mu\text{m}$ ($\lambda = 1.16$, Fig. 9(e)), this (reduction of h' by $\sim 50\%$, i.e. from 0.988 to 0.434) happens when $l = 17.7 \mu\text{m}$; at $s = 102.85 \mu\text{m}$ ($\lambda = 2.2$, Fig. 9(f)), this reduction of fill ratio by $\sim 50\%$ is expected to occur at $l > 17.7 \mu\text{m}$. This is consistent with experimental observations shown in Fig. 8 and Table 5. On the contrary, the punch width w has a similar but inversed effect on the fill ratio. To illustrate, data shown in Fig. 11(a) is interpolated and presented in a contour plot in Fig. 11(b). Each of the four probing arrows a_1 , a_2 , a_3 , and a_4 represent data corresponding to constant values of $s/l = 0.66, 2.06, 3.49$, and 5.02 , respectively. Along the arrows, w/l decreases monotonically from infinity to 2.64. It is evident that, at any given s/l , the fill ratio significantly increases as w/l decreases (i.e., as w approaches l).

3.4 Additional remarks

The plastic response of materials at small length scales has been the subject of intense study since the 1990s. Numerous papers have since been published on the theory, modeling, and simulations of strain gradient plasticity and dislocation dynamics and their relevance to plastic deformation at small scales. The experimental studies, while also abundant, have largely concentrated on a few deformation geometries, including wire torsion, foil bending, pillar compression, and Berkovich indentation. It is believed that the present experimental configuration of micron scale molding by rectangular punches provides an example involving complex plastic flows that is distinct from the ones listed above, against which small scale plasticity theories/models can be tested. The present micron scale molding example is not as relevant to dislocation-source-limited plastic response, as studied extensively in micro/nano sized pillar loadings [27, 28]. One kind of mechanical size effect is expressed by the surface layer model, which states that a layer next to the specimen free surface possesses a diminished flow stress as compared to that of the specimen interior [16]. This is also not as relevant to the present single- and double- punch molding experiments as plastic flow occurs predominantly within the material interior and not close to a free surface. We believe that the present experiments provide a good test case for SGP model and simulations. As such, it is hoped that the substantial amount of new data presented in this paper will be valuable for calibration/validation of new SGP models.

To the best of our knowledge, the present study documents two new experimental manifestations of plasticity size effects: 1) the dependence of the characteristic molding pressure p_c on the absolute gap size s and punch width w at identical relative punch dimensions $\lambda=s/w$; 2) the dependence of material flow to fill the gap between two punches on the absolute gap dimension s at identical λ .

From the perspective of SGP, the absolute length scale effects originate from the relative relation between s , w , and l . In the limit when both s/l and w/l approach infinity, the macroscopic conventional plasticity is recovered. As s/l and w/l approach unity, significant size effects ensue. In other words, the effects of variables s , w , and l on the materials response during the punch molding process is not completely independent. Rather, only two out of the three variables are independent. In the present set of experiments, size effects have been assessed by systematically varying s and w (while ensuring L is large enough such that no spurious effects arise due to the punch aspect ratio $\alpha=L/w$), as the intrinsic material length scale parameter l is considered to be fixed for a given material. In the present set of 2D double-punch simulations using SGP model (described in Table 2(a)), only s and l are varied while fixing $w=46.75\ \mu\text{m}$. In the data presented in Fig. 7(b), at each given λ value, the varying l from $0\ \mu\text{m}$ to $17.7\ \mu\text{m}$ represents the variation of w/l from infinity to 2.64. Therefore, the previous observations made in Fig. 7(b) on the effect of the intrinsic material length scale, when inversed, is applicable to the effect of the absolute characteristic deformation length scales (s and w) in the range of λ probed. When s and w approach l , the saturation of p_c with increasing λ is delayed. In addition, the overall molding pressure also elevates at smaller w and s with respect to l . The value of p_c , obtained at a depth of $l/w=0.18$, was plotted against w/l in Fig. 12(a) as a function of λ . A w/l value of 10^5 is chosen to represent the macroscopic conventional plastic behavior. It is noted that as the absolute value

of w —and therefore the absolute value of s at a fixed λ —decreases, the overall mechanical response stiffens. This trend is consistent with the experimental results, as demonstrated through four blue data points in Fig. 7(a), with λ fixed at 0.2.

To provide further insights on the effects of s/l and w/l , discrete data points presented in Fig. 7(b) are fitted with a double exponential function of the form $p_c = a \exp\left(-\exp\frac{\lambda-b}{c}\right) + d$, in which a and c are functions of l . Further details of the fit have been provided in Section S4 of Supplemental Materials. This fitting function describes the continuous variation of p_c as λ —therefore s —and l are independently varied, while w is fixed. This function is therefore capable of assessing the effect of s/l and w/l on p_c (Fig. 12(b)). Indeed, Fig. 12(b) indicates that—similar to the case of the die filling ratio shown in Fig. 11—both s/l and w/l affect p_c . Specifically, the following observations can be made from the simulation results:

1. at any given w/l , the characteristic molding pressure (p_c) experiences a step-like increase as a function of s/l ;
2. the value of s/l at which the p_c “jumps” increases with increasing w/l ;
3. the magnitude of the jump decreases with increasing w/l ; and
4. p_c remains a relatively constant value before and after the jump.

The FE simulations conducted in this work were not intended to exactly reproduce mechanical responses, such as the molding force and pressure, obtained from the punch molding experiments, as the materials behavior input into the simulations followed an idealized flow rule (Fig. 2(d)), not necessarily reflecting actual material behavior. Nevertheless, a first order approximation regarding the intrinsic material length scale parameter l of the physical Al specimen can be made by comparing the simulated die filling ratio with the experimental results. Experiments performed according to Table 1(c) maintained an almost constant punch width of $w \approx 5 \mu\text{m}$, and a varying λ from 0.2 to 1.5. An increasing die filling ratio was observed as λ increased. At $\lambda = 1.5$, the fill ratio is $h/l = 1$, corresponding to a $w/l = 23.4$ on Fig. 11, as marked by the blue dot. At $w = 5 \mu\text{m}$, the corresponding l is 214 nm. Alternatively, experiments performed according to Table 1(a) maintained a constant punch spacing of $s = 2 \mu\text{m}$, a varying w from 17 to 4.2 μm , and a varying λ from 0.12 to 0.48. The result is an increase in h/l from 0.04 to 0.32 with increasing λ . At $\lambda = 0.48$, the fill ratio is $h/l = 0.32$, corresponding to a $w/l = 20.3$ on Fig. 11, as marked by the green dot. At $w = 4.2 \mu\text{m}$, the corresponding l is 207 nm, which agrees well with the previous estimate of 214 nm. This value, $l \sim 210$ nm for the present Al specimen, is smaller than a previous assessment of l for Cu based on a confined shear experiment, which was ~ 650 nm [29]. Whether the intrinsic material length scale parameter determined from one group of experiments has applicability to a different group of experiments carried out on the same material but with distinctly different deformation geometries is key to assessing the predictive power of current SGP models. A definitive answer to this question remains to be offered through future studies combining additional experimentation with further plasticity simulations. Once the SGP model is validated, the model and associated simulations are expected to be able to guide further experimentation in different deformation geometries, e.g., multiple- instead of double- punch molding at the micron scale. Such work is also left for the future.

4 Summary

Instrumented microscale compression molding of a single-crystal Al specimen with single- and double- rectangular punches was conducted. Quantitative measurements of the molding force and material flow to fill the gap between the double-punches were carried out as a function of the punch width and gap spacing, and revealed new manifestations of plasticity size effects. A detailed set of 2D and 3D finite element simulations using both conventional and strain gradient plasticity models was performed, addressing the effects of punch aspect ratio, spacing, and width, as well as the intrinsic material length scale parameter. These simulations complement the experimental results and offer insights into how material flow is impacted when the characteristic dimensions of deformation approach the intrinsic material length scale. The present study is relevant to the technology of microscale pattern replication on metal surfaces, and offers a distinct experimental case study in which plasticity size effects dominate the efficacy of pattern replication by molding at the micron scale.

Supplementary Material

Refer to Web version on PubMed Central for supplementary material.

Acknowledgements

The authors gratefully acknowledge partial project support from the U.S. National Science Foundation (NSF OIA-1541079). The experimental work used facilities at the LSU shared instrumentation facility (SIF), a part of the NSF EPSCoR CIMM core user facilities (CUF). This material, in part, is based upon work supported by the U.S. Department of Energy, Office of Science, Office of Basic Energy Sciences, under Award Number DE-SC0019378. The authors thank Prof. Emilio Martínez Pañeda for kindly providing the UMAT subroutine for strain gradient plasticity and helpful discussions. This research was performed in part as a collaborative project with the P41 Center for BioModular Multiscale Systems for Precision Medicine from the U.S. National Institutes of Health (NIH P41EB020594).

9. References:

- [1]. Hosomi K, Kikawa T, Goto S, Yamada H, Katsuyama T, Arakawa Y. Ultrahigh-aspect-ratio SiO₂ deeply etched periodic structures with smooth surfaces for photonics applications. *J Vac Sci Technol B* 2006;24:1226–9.
- [2]. Schmidt V, Riel H, Senz S, Karg S, Riess W, Gösele U. Realization of a silicon nanowire vertical surround-gate field-effect transistor. *Small* 2006;2:85–8. [PubMed: 17193560]
- [3]. Fletcher PDI, Haswell SJ, Pombo-Villar E, Warrington BH, Watts P, Wong SYF. Micro reactors: principles and applications in organic synthesis. *Tetrahedron* 2002;58:4735–57.
- [4]. Mei F, Parida PR, Jiang J, Meng WJ, Ekkad SV. Fabrication, assembly, and testing of Cu-and Al-based microchannel heat exchangers. *J Microelectromechanical Syst* 2008;17:869–81.
- [5]. Backer EW, Ehrfeld W, Münchmeyer D, Betz H, Heuberger A, Pongratz S. Production of separation-nozzle systems for uranium enrichment by a combination of X-ray lithography and galvanoplastics. *Naturwissenschaften* 1982;69:520–3.
- [6]. Chou SY, Krauss PR, Renstrom PJ. Nanoimprint lithography. *J Vac Sci Technol B* 1996;14:4129–33.
- [7]. Cao DM, Meng WJ. Microscale compression molding of Al with surface engineered LiGA inserts. *Microsyst Technol* 2004;10:662–70.
- [8]. Cao DM, Jiang J, Meng WJ, Jiang JC, Wang W. Fabrication of high-aspect-ratio microscale Ta mold inserts with micro electrical discharge machining. *Microsyst Technol* 2007;13:503–10.
- [9]. Jiang J, Mei F, Meng WJ. Fabrication of metal-based high-aspect-ratio microscale structures by compression molding. *J Vac Sci Technol A* 2008;26:745–51.

- [10]. Lu B, Chen K, Meng WJ, Mei F. Fabrication, assembly and heat transfer testing of low-profile copper-based microchannel heat exchangers. *J Micromechanics Microengineering* 2010;20:115002.
- [11]. Lu B, Meng WJ, Mei F. Experimental investigation of Cu-based, double-layered, microchannel heat exchangers. *J Micromechanics Microengineering* 2013;23:35017.
- [12]. Zhang B, Ahmed S, Shao S, Meng WJ. Mechanical response of mesoscopic aluminum rings under uniaxial compression. *MRS Commun* 2018;8:1254–60.
- [13]. Fleck NA, Muller GM, Ashby MF, Hutchinson JW. Strain gradient plasticity: theory and experiment. *Acta Metall Mater* 1994;42:475–87.
- [14]. Stölken JS, Evans AG. A microbend test method for measuring the plasticity length scale. *Acta Mater* 1998;46:5109–15.
- [15]. Uchic MD, Dimiduk DM, Florando JN, Nix WD. Sample dimensions influence strength and crystal plasticity. *Science* (80-) 2004;305:986–9.
- [16]. Engel U, Eckstein R. Microforming—from basic research to its realization. *J Mater Process Technol* 2002;125–126:35–44.
- [17]. Fu MW, Chan WL. A review on the state-of-the-art microforming technologies. *Int J Adv Manuf Technol* 2013;67:2411–37.
- [18]. Ghassemali E, Tan M-J, Lim SCV, Wah CB, Jarfors AEW. Experimental and simulation of friction effects in an open-die microforging/extrusion process, *J Micro Nano Manufact* 2014;2:011005/1–12.
- [19]. Chen K, Meng WJ, Mei F, Hiller J, Miller DJ. From micro-to nano-scale molding of metals: Size effect during molding of single crystal Al with rectangular strip punches. *Acta Mater* 2011;59:1112–20.
- [20]. Jiang J, Sinclair GB, Meng WJ. Quasi-static normal indentation of an elasto-plastic substrate by a periodic array of elastic strip punches. *Int J Solids Struct* 2009;46:3677–93.
- [21]. Jiang J, Meng WJ, Sinclair GB, Lara-Curzio E. Further experiments and modeling for microscale compression molding of metals at elevated temperatures. *J Mater Res* 2007;22:1839–48.
- [22]. Camacho AM, Veganzones M, Claver J, Martín F, Sevilla L, Sebastián MA. Determination of actual friction factors in metal forming under heavy loaded regimes combining experimental and numerical analysis. *Materials* 2016;9:751/1–16.
- [23]. Schrader T, Shirgaokar M, Altan T. A critical evaluation of the double cup extrusion test for selection of cold forging lubricants. *J. Mater. Process. Technol.* 2007;189:36–44.
- [24]. Huang Y, Qu S, Hwang KC, Li M, Gao H. A conventional theory of mechanism-based strain gradient plasticity. *Int J Plast* 2004;20:753–82.
- [25]. Martínez-Pañeda E, Betegón C. Modeling damage and fracture within strain-gradient plasticity. *Int J Solids Struct* 2015;59:208–15.
- [26]. Martin H *Elasticity-Theory, Applications, and Numerics*. Elsevier Science Publishing Company; 2014.
- [27]. Shao S, Abdolrahim N, Bahr DF, Lin G, Zbib HM. Stochastic effects in plasticity in small volumes. *Int J Plast* 2014;52:117–32.
- [28]. Uchic MD, Shade PA, Dimiduk DM. Plasticity of micrometer-scale single crystals in compression. *Annu Rev Mater Res* 2009;39:361–86.
- [29]. Mu Y, Hutchinson JW, Meng WJ. Micro-pillar measurements of plasticity in confined Cu thin films. *Extrem Mech Lett* 2014;1:62–9.

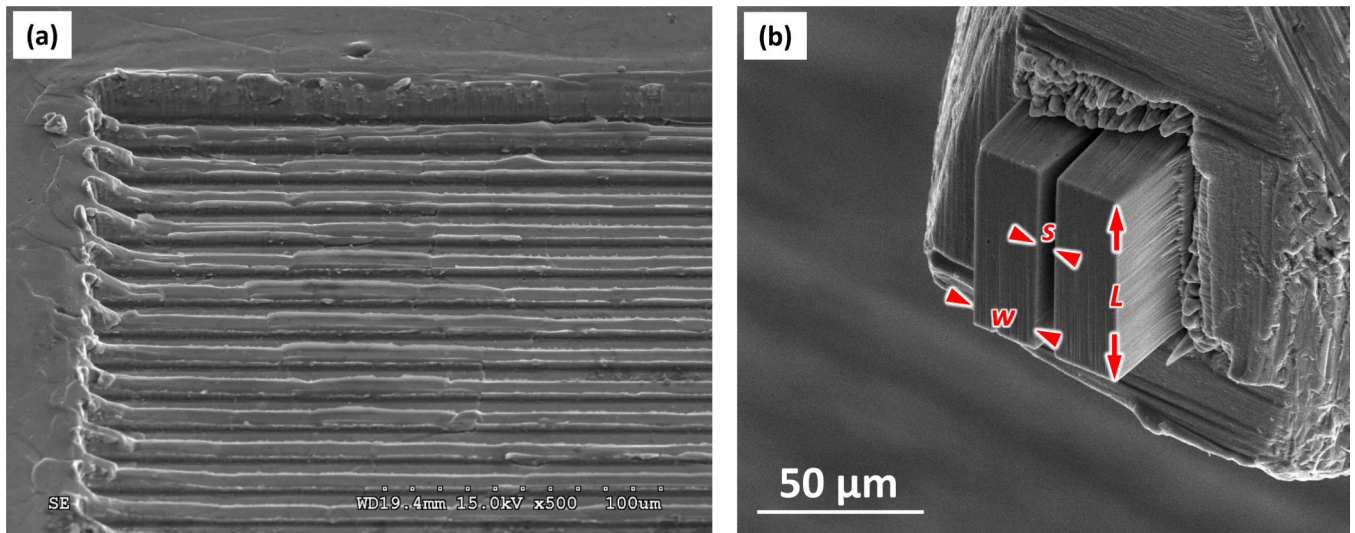


Fig. 1.

(a) an SEM image showing a 50° tilt view of a bulk piece of Al after compression molding with a Si die consisting of a one-dimensional periodic array of long rectangular Si punches, all with the same height. The width of each Si punch is $\sim 9\mu\text{m}$, and the gaps between punches are $\sim 9\mu\text{m}$. Incomplete Al filling of gaps between Si punches are evident; (b) one FIB-milled tool steel double-punch used in the present work to study the mechanical response and punch gap filling by Al during molding, with a length L of $\sim 67\mu\text{m}$, a width w of $\sim 22.5\mu\text{m}$, and a spacing between the two punches s of $\sim 4.5\mu\text{m}$.

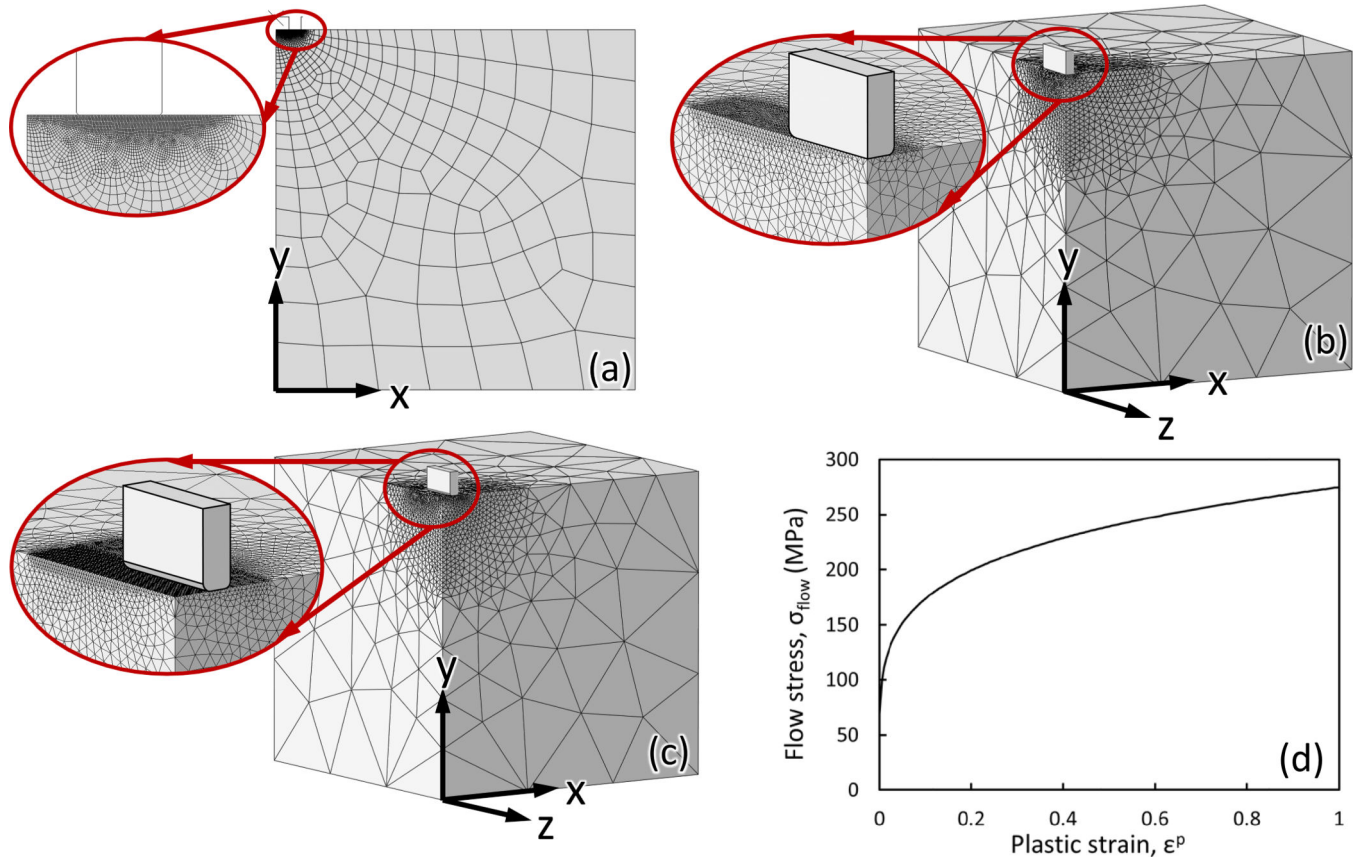


Fig. 2. (a) 2D plane-strain mesh for double-punch FE simulations; (b) 3D mesh for single-punch FE simulations; (c) 3D mesh for double-punch FE simulations; (d) flow stress – plastic strain response produced by the adopted SGP model, setting $l = 0$.

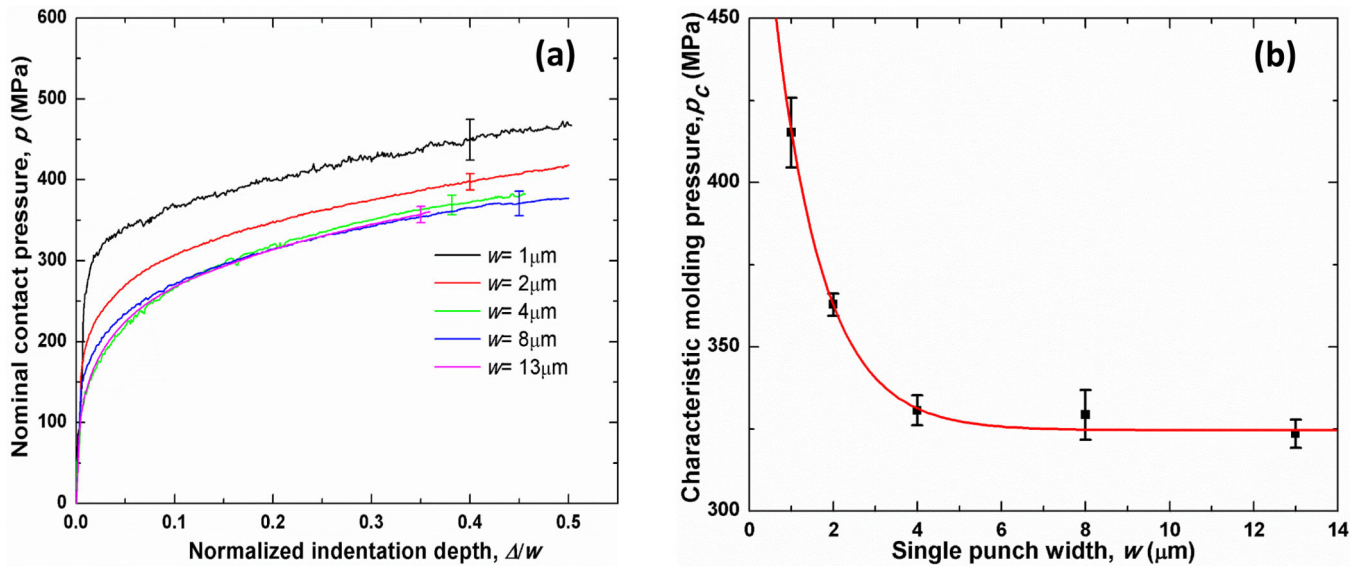


Fig. 3. Mechanical size effect in rectangular single-punch molding: (a) the averaged nominal contact pressure vs. the normalized indentation depth at different punch widths; (b) the characteristic molding pressure as a function of the punch width. The red line is a guide to the eye.

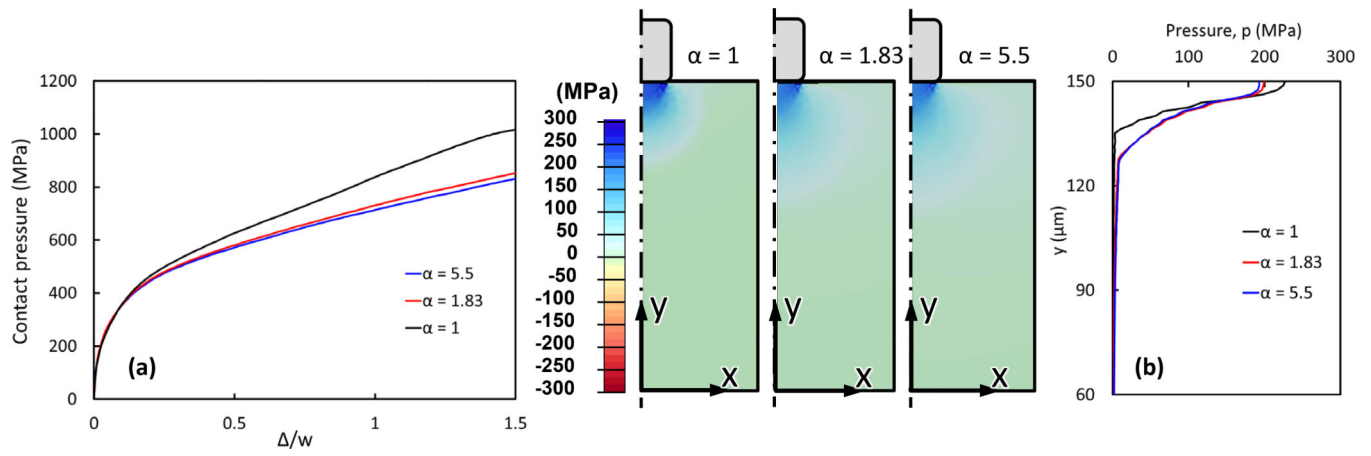


Fig. 4.

(a) The effect of punch aspect ratio on the pressure-depth response obtained from 3D FE simulations; (b) distribution of pressure (mean stress) below single punches on the x-y plane as well as along the y-axis.

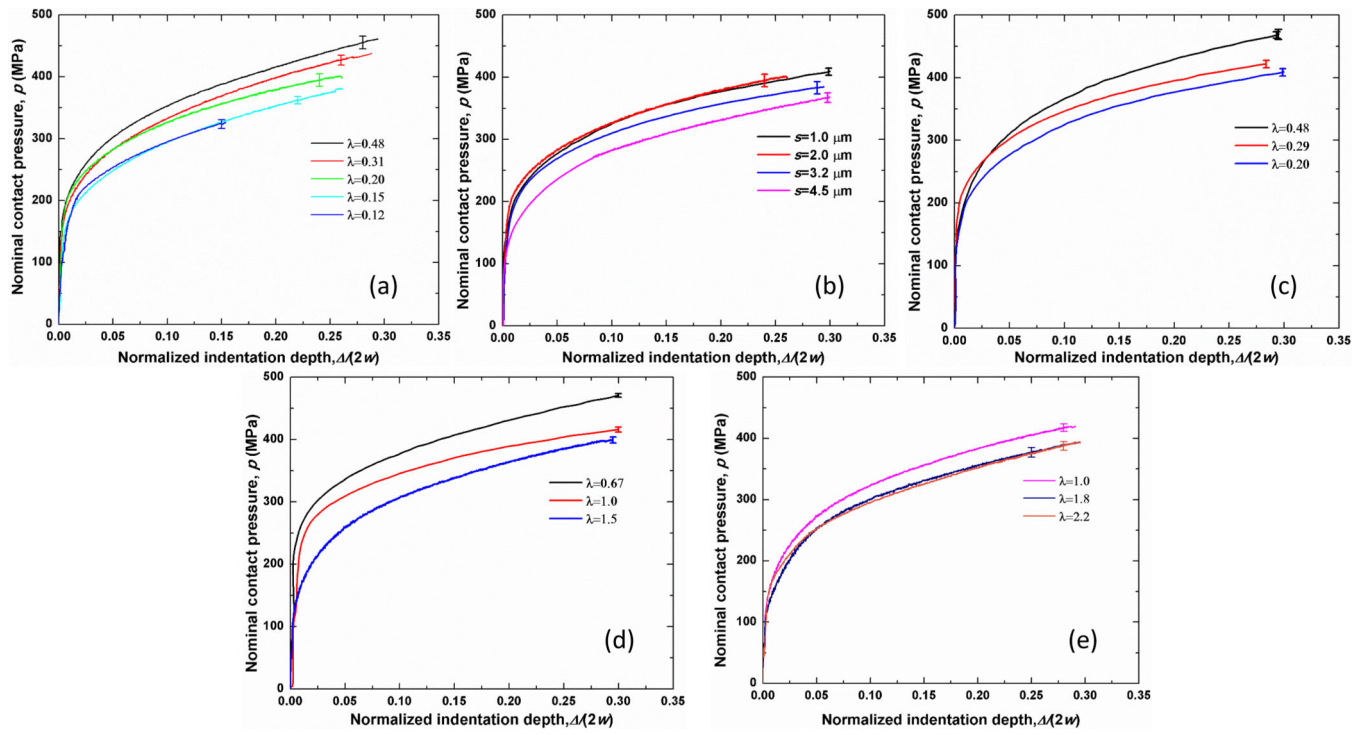


Fig. 5. Molding response curves measured using various double-punches: p - $\Delta/2w$ curves obtained from double-punches listed in (a) Table 1(a); (b) Table 1(b); (c)/(d) Table 1(c); (e) Table 1(d).

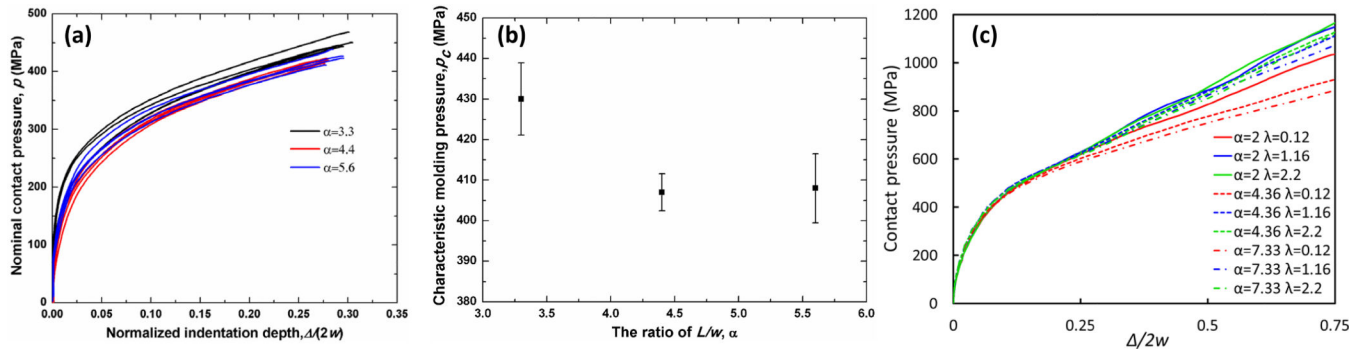


Fig. 6.

Punch aspect ratio effects in double-punch molding: from experiments: (a) nominal contact pressure vs. normalized indentation depth curves at different α values; (b) the characteristic molding pressure as a function of α ; from simulations: (c) contact pressure vs. normalized indentation depth curves at different α and λ values.

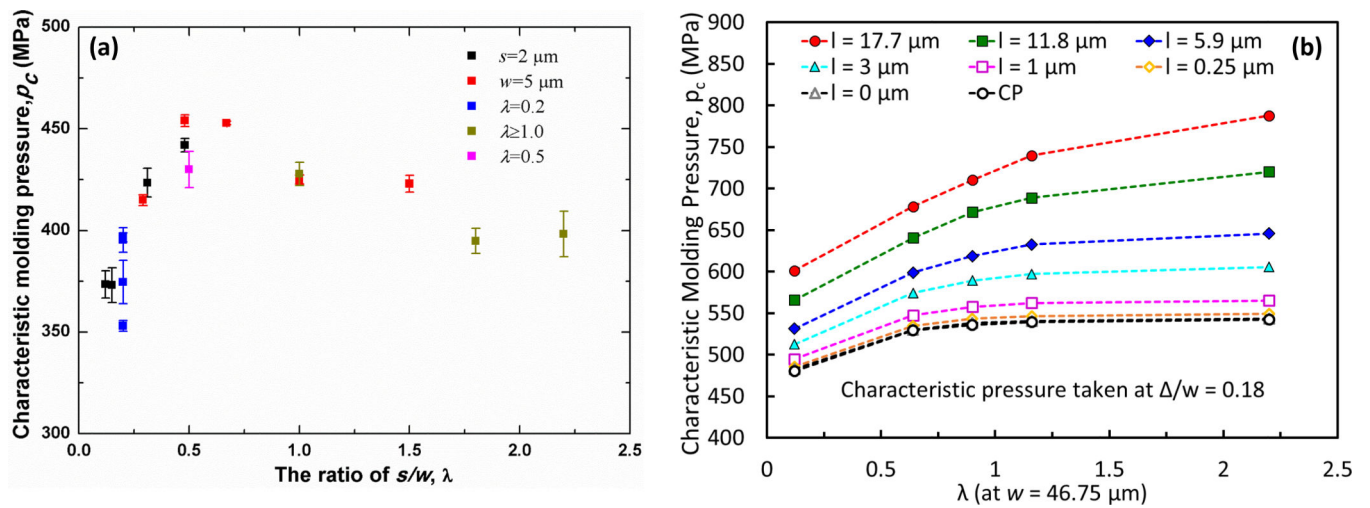


Fig. 7.

(a) Experimental results of double-punch characteristic molding pressure vs. λ . The “ $s=2\ \mu\text{m}$ ”, “ $\lambda=0.2$ ”, “ $w=5\ \mu\text{m}$ ”, “ $\lambda=1.0$ ”, and “ $\lambda=0.5$ ” data groups correspond to data shown Figs. 5(a), 5(b), 5(c)/5(d), 5(e) and Fig. 6(a), respectively. Correction to p_c values due to varying punch aspect ratio $\alpha=L/w$ was done according to data presented in Fig. 6; (b) corresponding p_c - λ data obtained from 2D plane-strain FE simulations with both CP and SGP with varying values of l .

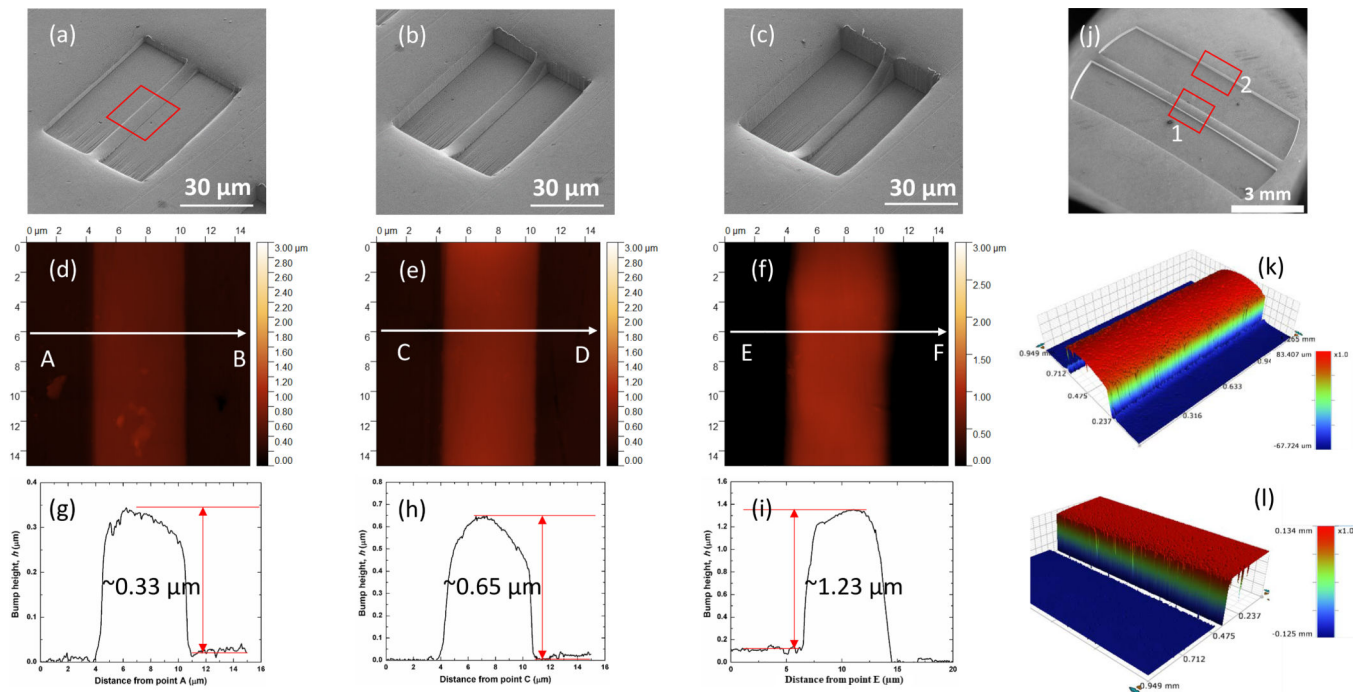


Fig 8. Incomplete die filling in double-punch molding of Al: (a)/(b)/(c) SEM images of micro-imprints made respectively at of $\sim 3.5 \mu\text{m}$, $\sim 8.8 \mu\text{m}$, and $11.8 \mu\text{m}$; (d)/(e)/(f) $15 \mu\text{m} \times 15 \mu\text{m}$ AFM scans taken respectively from imprint center regions shown in (a)/(b)/(c), indicated schematically in (a); (g)/(h)/(i) AFM line profiles taken respectively from line traces marked A to B, C to D, and E to F in (d)/(e)/(f); (j) SEM of a macro-imprint made at of $\sim 230 \mu\text{m}$; (k)/(l) OP scans of areas marked 1 and 2 in (j).

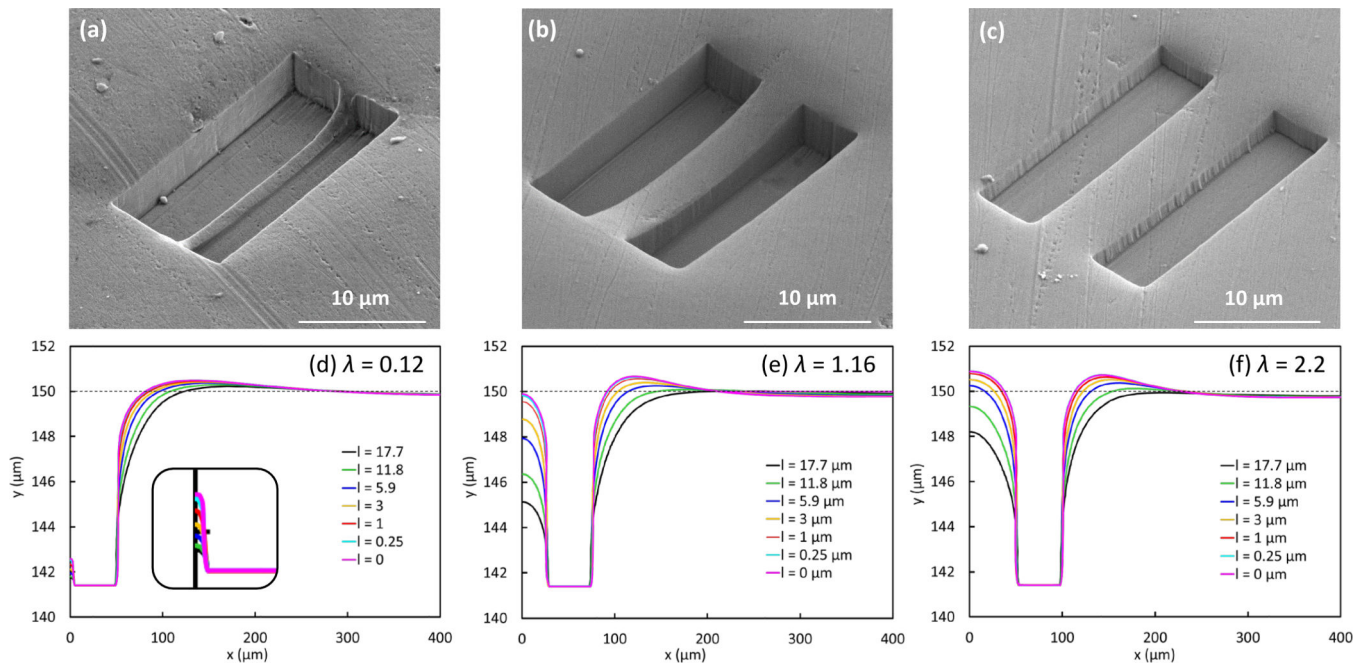


Fig 9. SEM images of three micron-scale double-punch molding imprints for the case of (a) $w=5 \mu\text{m}$, $s=1.0 \mu\text{m}$; (b) $w=5.2 \mu\text{m}$, $s=3.5 \mu\text{m}$; (c) $w=5.2 \mu\text{m}$, $s=5.2 \mu\text{m}$. Surface profile plots of 2D FE simulations with SGP. The maximum molding displacement is $8.9 \mu\text{m}$ and the punch width is $w = 46.75 \mu\text{m}$: (d), (e), and (f) correspond respectively to $\lambda = 0.12$, 1.16 , and 2.2 . Curves with different color correspond to different values of the intrinsic material length scale parameter, l . The Inset in (d) shows the magnified view at the region between the punches.

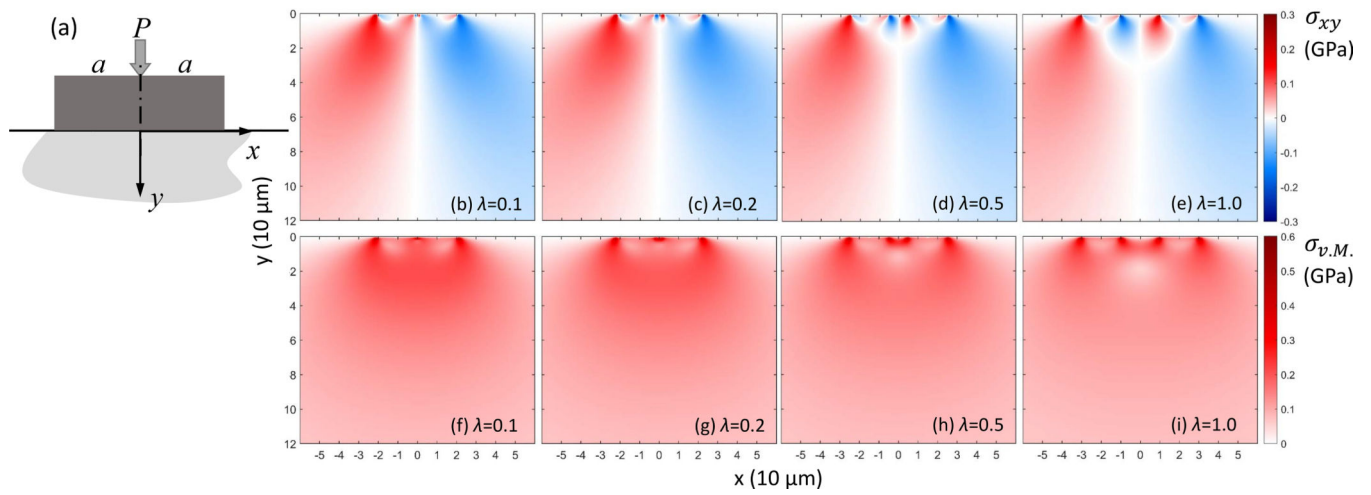


Fig 10. Isotropic, plane-strain, linear elastic solution of double-punch loading: (a) is a schematic drawing of single-punch loading, (b)–(e) show the distribution of the shear stress σ_{xy} , (f)–(i) show the distribution of the von Mises stress $\sigma_{v.M.}$ for double-punch loading.

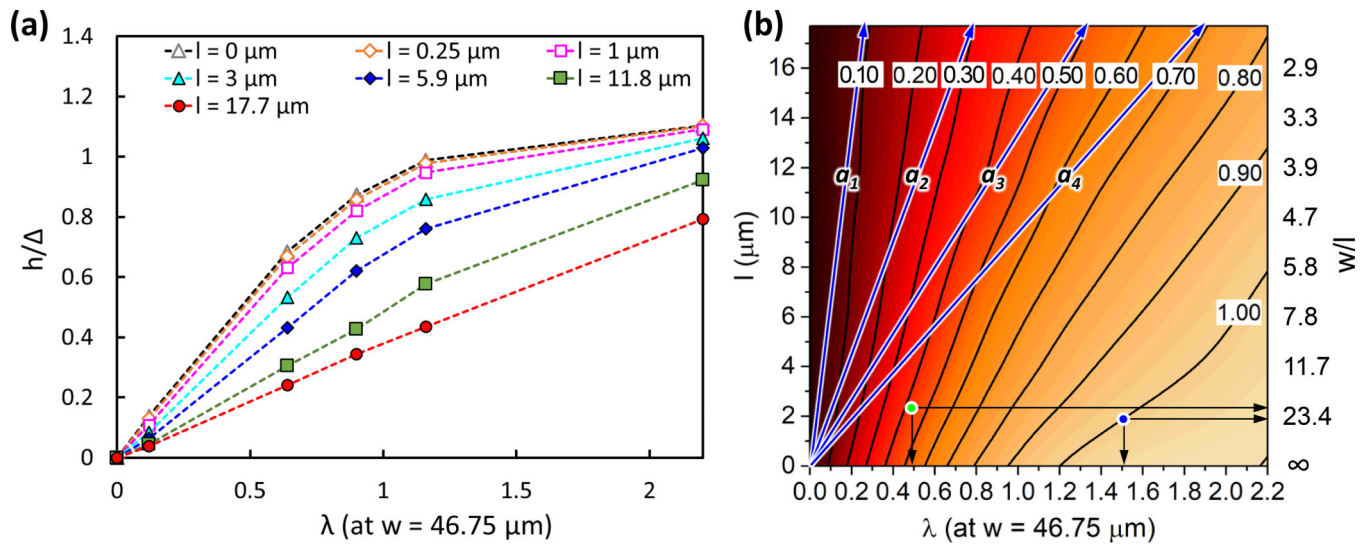


Fig 11.
 (a) Values of the gap filling ratio from 2D double-punch simulations as a function of λ . The data points are obtained at $w = 46.75 \mu\text{m}$ and $l/w = 0.18$; (b) contour plot of h/Δ corresponding to the data shown in (a). Color changes, from black to red to yellow, represent the variation in h/Δ . The right vertical axis gives the values of w/l corresponding to the change in l .

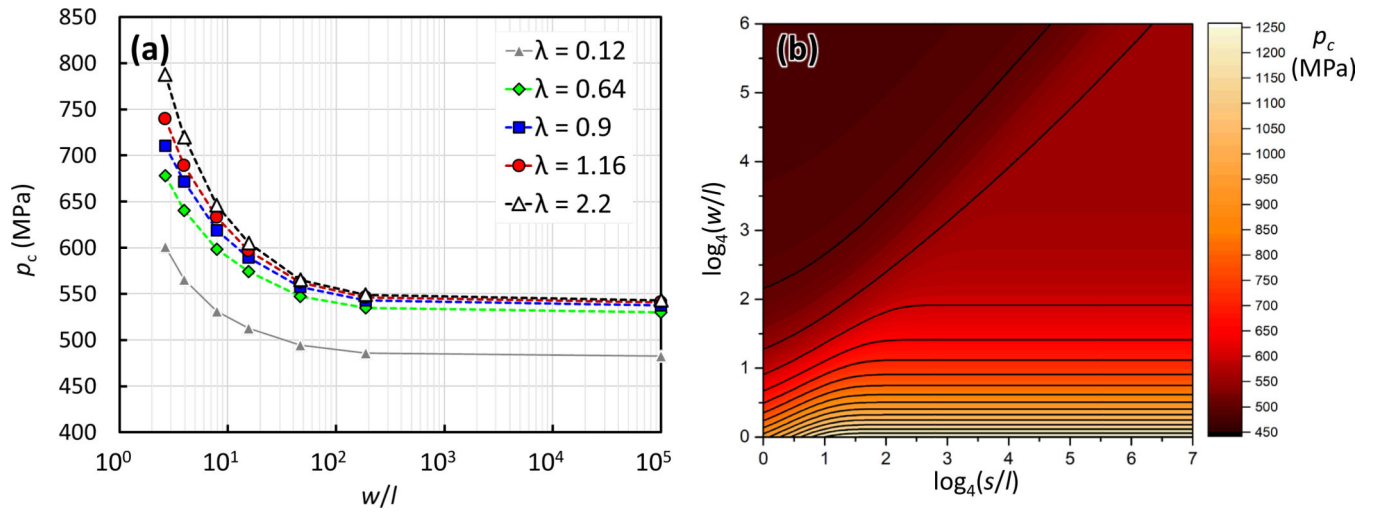


Fig 12.

(a) Plots of double-punch p_c values as functions of w/l using data presented in Fig. 7(b); (b) a contour plot of p_c as functions of both $\log_4(w/l)$ and $\log_4(s/l)$.

Table 1.

Dimensions of FIB-cut double-punches fabricated for the present study. The two bold entries in 1(b) signifies that they appear again in 1(a) and 1(c), and the corresponding entries in 1(a) and 1(c) are denoted by parenthesis.

	1(a): s fixed at $\sim 2 \mu\text{m}$ while λ varies					1(b): λ fixed at ~ 0.2 while s and w vary			
$s (\mu\text{m})$	2.0	2.0	(2.0)	2.0	2.0	1.0	2.0	3.2	4.5
$w (\mu\text{m})$	17.0	13.0	(10.2)	6.5	4.2	5.0	10.2	16.0	22.5
$L (\mu\text{m})$	53.0	50.0	(35.0)	21.0	14.0	19.0	35.0	51.0	67.0
$\lambda = s/w$	0.12	0.15	(0.20)	0.31	0.48	0.20	0.20	0.20	0.20
$\alpha = L/w$	3.1	3.8	(3.4)	3.2	3.3	3.8	3.4	3.2	3.0
	1(c): w fixed at $\sim 5 \mu\text{m}$					1(d): s and w both vary			
$s (\mu\text{m})$	(1.0)	1.5	2.4	3.5	5.2	7.5	6.0	7.6	8
$w (\mu\text{m})$	(5.0)	5.2	5.0	5.2	5.2	5.0	6.0	4.3	3.6
$L (\mu\text{m})$	(19.0)	17.5	17.3	20.0	23.0	24.0	39.0	23.8	18.0
$\lambda = s/w$	(0.20)	0.29	0.48	0.67	1.0	1.5	1.0	1.8	2.2
$\alpha = L/w$	(3.8)	3.4	3.5	3.8	4.4	4.8	6.5	5.5	5.0

Table 2.

A summary of CP and SGP FE simulations performed in the present study.

2(a). List of 2D double-punch FE simulations with CP and SGP.

$w = 46.75 \mu\text{m}$ $\lambda = s/w$	CP	SGP: Intrinsic material length scale, l (μm)						
		0	0.25	1	3	5.9	11.8	17.7
0.12	✓	✓	✓	✓	✓	✓	✓	✓
0.64	✓	✓	✓	✓	✓	✓	✓	✓
0.9	✓	✓	✓	✓	✓	✓	✓	✓
1.16	✓	✓	✓	✓	✓	✓	✓	✓
2.2	✓	✓	✓	✓	✓	✓	✓	✓

2(b). List of 3D single- and double- punch CP simulations.

$\lambda = s/w$	Aspect ratio, $a=L/w$					
	7.33	5.5	4.36	2	1.83	1
0.12	✓		✓	✓		
double-punch $w = 5.5 \mu\text{m}$ 1.16	✓		✓	✓		
2.2	✓		✓	✓		
single-punch $w = 11 \mu\text{m}$ ---		✓			✓	✓

Table 3.

Values of material parameters used in the FE simulations, including Young's modulus (E), Poisson's ratio (ν), yield stress (σ_y), intrinsic material length scale (l), and strain hardening exponent (N).

E (GPa)	ν	σ_y (MPa)	l (μm)	N
69	0.3	69	0 – 17.7	0.2

Author Manuscript

Author Manuscript

Author Manuscript

Author Manuscript

Table 4.

Dimensions of double-punches with a fixed s of $\sim 3.6 \mu\text{m}$ and w of $\sim 7.2 \mu\text{m}$, but different α values.

$s (\mu\text{m})$	3.6	3.6	3.6
$w (\mu\text{m})$	7.2	7.2	7.2
$L (\mu\text{m})$	40	32	24
$\lambda = s/w$	0.5	0.5	0.5
$\alpha = L/w$	5.6	4.4	3.3

Author Manuscript

Author Manuscript

Author Manuscript

Author Manuscript

Table 5.

Incomplete gap filling in micro- and macro- scale double-punch molding.

	$s = 4.5 \mu\text{m}, w = 22.5 \mu\text{m}$			$s = 400 \mu\text{m}, w = 2000 \mu\text{m}$		
<i>Indentation depth, (μm)</i>	3.5	8.8	11.8	88	230	380
<i>Bump height, h (μm)</i>	0.33	0.65	1.23	23	145	228
<i>$h/$</i>	0.09	0.07	0.1	0.26	0.63	0.60

Author Manuscript

Author Manuscript

Author Manuscript

Author Manuscript